Model Study of Waves Generated by Convection with Direct Validation via Satellite

ALISON W. GRIMSDELL AND M. JOAN ALEXANDER

NorthWest Research Associates, Colorado Research Associates Division, Boulder, Colorado

PETER T. MAY

Centre for Australian Weather and Climate Research, CSIRO/Bureau of Meteorology, Melbourne, Victoria, Australia

LARS HOFFMANN

Forschungszentrum Jülich, ICG-1, Jülich, Germany

(Manuscript received 12 May 2009, in final form 28 September 2009)

ABSTRACT

Atmospheric gravity waves have a major effect on atmospheric circulation, structure, and stability on a global scale. Gravity waves can be generated by convection, but in many cases it is difficult to link convection directly to a specific wave event. In this research, the authors examine an event on 12 January 2003 when convective waves were clearly generated by a period of extremely intense rainfall in the region of Darwin, Australia, during the early morning. The waves were observed by the Atmospheric Infrared Sounder (AIRS) instrument on board the *Aqua* satellite, and a dry version of a nonlinear, three-dimensional mesoscale cloud-resolving model is used to generate a comparable wave field. The model is forced by a spatially and temporally varying heating field obtained from a scanning radar located north of Darwin at Gunn Point. With typical cloud-resolving model studies it is generally not possible to compare the model results feature-for-feature with observations since although the model precipitation and small-scale heating may be similar to observations, they will occur at different locations and times. In this case the comparison is possible since the model is forced by the observed heating pattern. It is shown that the model output wave pattern corresponds well to the wave pattern observed by the AIRS instrument at the time of the AIRS overpass.

1. Introduction

Small-scale gravity waves are a common feature of the middle atmosphere (altitudes ranging from ~10 to 100 km) and are known to play an important role in shaping the mean flow in this region (Vincent and Reid 1983; Nastrom and Gage 1985; Fritts and Alexander 2003). In the tropics, gravity waves appear to provide the major contribution to forcing both the quasi-biennial oscillation (QBO) and the semiannual oscillation (SAO) (Hamilton et al. 2004; Dunkerton 1997; Giorgetta et al. 2002).

There are many different sources of atmospheric gravity waves, the most obvious being topography, convection, fronts, regions of imbalance within the jet stream, and shear. Understanding these sources and their generation mechanisms is crucial to successfully modeling the general circulation of the middle atmosphere (Pandya and Alexander 1999; Charron and Manzini 2002; Beres et al. 2005). The source of the waves influences the behavior of the wave field produced; for example, the source region for topographically produced waves does not move, so mountain waves have phase speeds near zero. In contrast, for convectively generated waves the source can vary in both time and space, generating waves with a wider range of phase speeds, frequencies, and vertical and horizontal scales (Fritts and Alexander 2003).

Convection as a source of gravity waves has been modeled and studied for many years (Fovell et al. 1992; Alexander et al. 1995), and convection is a particularly important source in the tropics (Chun and Baik 1998). The region of influence of convective clouds can be much larger than the actual cloud cover: while the dynamical scale of cumulonimbus is on the order of 10 km, the scale

Corresponding author address: Alison Grimsdell, NWRA, CoRA Division, 3380 Mitchell Lane, Boulder, CO 80301.
E-mail: grimsdell@cora.nwra.com

of the accompanying convectively driven circulation can be hundreds of kilometers (Wu and Moncrieff 1996). The waves generated have a significant impact on global atmospheric circulation. The tropical QBO is understood to be an important component of interannual variability in middle atmospheric climate, with effects felt even in the extratropics and polar regions (Baldwin et al. 2001). Model studies have shown that mesoscale gravity waves generated by convection may provide ~30%–50% of the zonal forcing required for the QBO (Piani et al. 2000; Giorgetta et al. 2002).

Within the middle atmosphere the response to gravity waves is complex, including propagation vertically and horizontally, dissipation, and nonlinear interactions. Gravity waves transport vertical flux of horizontal momentum through the atmosphere and dissipate at higher levels. In this way, waves generated in the troposphere can exert a significant acceleration or deceleration on the flow aloft, including and above the stratosphere, and can profoundly influence the flows of momentum, energy, and constituents on a global basis (Holton 1983; Kershaw 1995). Atmospheric gravity waves naturally grow in amplitude with height, so long as the dissipation is not too strong, because of conservation of energy and the exponential decrease in atmospheric density with height (Fritts and Alexander 2003).

For global circulation studies, parameterizations have been developed for the momentum flux spectrum and mean-flow forcing due to convective waves (Chun et al. 2001; Beres et al. 2005). These are based on the linear theory for wave generation by localized, time-varying heat sources. There is currently scant observational evidence available to validate these parameterization schemes.

In this research we use a three-dimensional (3D), nonlinear, nonhydrostatic, cloud-resolving model forced by time-varying 3D latent heat derived from high-resolution scanning radar observations. Since the model is nonlinear, the dynamic and thermodynamic variables are coupled through the heat and momentum fluxes. The ability to force the model with the observed heating pattern gives us both an understanding of the mechanism of wave generation and the means to validate the model results with satellite data. We present a comparison between the model-generated wave field and that observed by the Atmospheric Infrared Sounder (AIRS) instrument on the *Aqua* satellite. The comparison provides a validation of the model method of forcing the waves with a prescribed heating field. The model method further provides a means of evaluating and improving the parameterizations developed for global model studies (Alexander et al. 2006).

In the past, diabatic or latent heating has been used as the forcing in many studies of wave generation by con-

vection (e.g., Bergman and Salby 1994; Ricciardulli and Garcia 2000). The heating in these studies was derived from satellite infrared cloud imagery or parameterized convection in climate models, which limited the wave properties to long time periods and large horizontal-scale wavelengths. Our method, using high-resolution radar data, allows us to study much shorter horizontal wavelengths and periods.

Another approach for short wavelength and period waves has been to study waves generated in cloud-resolving weather prediction models with microphysics (e.g., Kuester et al. 2008), but this approach cannot reproduce the feature-for-feature accuracy in the precipitation field that would be necessary to find a match between the waves in the model and the waves observed by the satellite. Wave generation is dependent on brief, intense, and highly localized rain events, which can only be reproduced in a general statistical sense in these more complex models, not in a feature-for-feature matched sense. Feature-for-feature matching in both space and time is required for direct validation with the satellite observation. Our method—forcing the model with heating from observed precipitation patterns—does allow a direct comparison to the AIRS satellite observation of the same gravity wave event.

A description of the AIRS instrument is given in section 2 as well as a brief description of the forward model. The forward model is used to convert the model output field from temperature to radiances so that a direct comparison can be made with the observed AIRS radiances. Section 3 gives details of the computer model, including a description of the forcing and model initialization, and details of the meteorology on the specific day used for comparison to the satellite image. Results from the model run are shown in section 4, and the discussion and conclusions are given in section 5.

2. AIRS

The *Aqua* satellite is part of the National Aeronautics and Space Administration's (NASA's) A-Train, a series of five satellites in high-inclination, sun-synchronous orbits designed to study the earth's atmosphere, oceans, and land surfaces, and their relationship to the changes in the earth system. The satellites orbit within 15 min of each other at an altitude of 705 km, with an orbital period of 98.8 min and an inclination of $98.2 \pm 0.1°$. *Aqua* is the lead satellite, and the largest. It crosses the equator at about 1:30 p.m. local solar time on ascending passes and 1:30 a.m. on descending passes. *Aqua* was launched on 4 May 2002 from Vandenberg Air Force Base as part of NASA's Earth Observing System (EOS).

AIRS is one of six instruments on board the *Aqua* satellite and provides vertical profiles of temperature
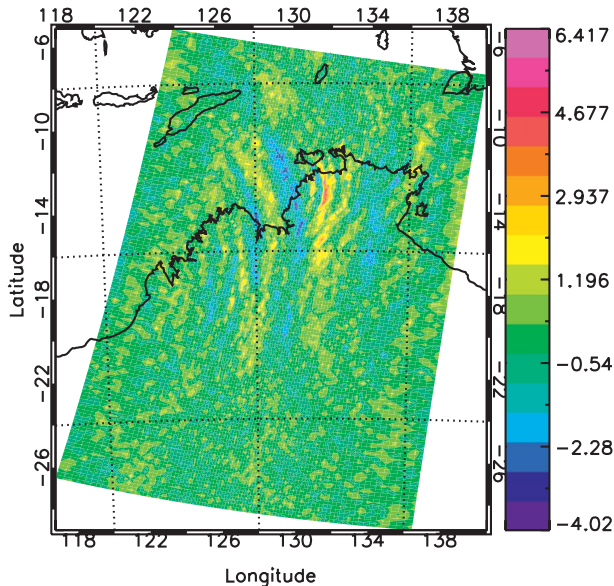
FIG. 1. AIRS radiance perturbations, defined as the difference from a fourth-order polynomial fit in scan angle that removes the scan angle dependent radiance. This is a granule from channel 75, in the 15-μm region, centered on wavenumber 667.78 cm^{-1}. The data were acquired over northern Australia at 1640 UTC 12 Jan 2003 and the radiance units are mW m^{-2} sr^{-1} cm.

and moisture, derived from the observed radiances. It has 2378 infrared spectral channels covering the range from 3.7 to 15.4 μm. The AIRS infrared channels have an instrument field of view of 1.1° and the scan angle extends to ±49.5° from nadir. The instrument scans perpendicular to the spacecraft ground track with a swath width of 1650 km and a horizontal resolution of 13.5 km at nadir. Each footprint takes 22.31 ms to acquire and there are 90 footprints across the flight track, plus calibration views every scan cycle, so that a full scan takes 2.67 s. Once 135 scans have been completed, these are assembled into an image called a granule, an example of which is given in Fig. 1 for AIRS channel 75.

AIRS temperature retrievals combine the infrared radiance measurements with collocated microwave measurements from the Advanced Microwave Sounding Unit (AMSU). AMSU footprints cover nine AIRS footprints, so the horizontal resolution of the temperature retrievals is a factor of 3 coarser in both horizontal dimensions than the AIRS radiance measurements. This means that while the average resolution in the AIRS radiances is ~20 km, this is degraded in the temperature retrievals to ~60 km. In the radiance image of Fig. 1 the wave perturbations of interest in this study have peaks reaching up to 6.4 mW m^{-2} sr^{-1} cm and are visible at around 13°S, 132°E. Since these waves are small in scale they are not visible in the temperature data; for this reason, we focus on the AIRS radiance measurements.

The direction of propagation of the waves can be inferred from the curvature in the phase lines (Taylor and Hapgood 1988; Dewan et al. 1998), which can be thought of as roughly concentric about the wave source below. In Fig. 1 the waves we are studying can be seen to have originated not far from Darwin, Australia (Darwin is located at 12.4°S, 130.9°E). A second set of waves is also visible in the image just to the west of Darwin, west of 130°E and between 10° and 20°S. These waves have a smaller amplitude than the waves we are studying, as well as less curvature of the wave fronts. From the curvature of the wave fronts we expect the source for this second set of waves to be well to the southwest of our study domain. Since we have detailed precipitation observations from only a small region near Darwin with which to drive the model, these waves cannot be reproduced in the model output wave field.

The kernel function for each channel of the AIRS instrument describes the sensitivity of the radiance observations to perturbations in the temperature profile. It determines the altitude and vertical resolution of the measurement. For this research we are using AIRS channel 75, which is within the 15-μm CO$_2$ band and is centered at wavenumber 667.78 cm^{-1} (wavelength = 14.9 μm). The kernel function for channel 75, calculated using a climatological tropical temperature profile, is shown in Fig. 2. The peak of the kernel function is at an altitude of ~41–43 km. The exact altitude of the peak varies depending on the temperature profile, and for this research we have compared the results at 41 km. In channel 75, very little information is included from below 30 km. Since this is above the tropopause, clouds do not influence the measurement. The noise for a single measurement in this channel is around 0.51 mW m^{-2} sr^{-1} cm.

a. Measurement characteristics

The range of gravity wave wavelengths visible to the satellite instrument is determined by the vertical and horizontal resolution of the satellite instrument as well as the atmospheric wind profile. The region of the AIRS image we are examining is near the center of the scans, where the horizontal resolution is about 14 km. The vertical resolution is determined by the depth of the kernel functions and the viewing geometry. For AIRS the viewing angles are near nadir and this fact, combined with the shapes of the kernel functions, means that it is very difficult to detect waves with vertical wavelengths not significantly larger than the full width at half maximum (FWHM) of the channel, which in this study is ~12–13 km (Alexander and Barnet 2007).

The wind profile affects the visibility of the waves to the satellite because as the waves travel upwind into
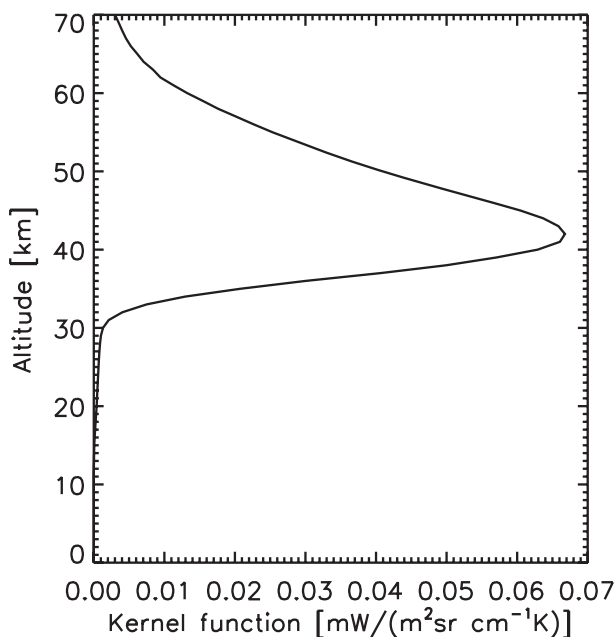
FIG. 2. The temperature kernel function for AIRS channel 75.

winds that increase in speed with height, the waves are refracted to longer vertical wavelengths that are more visible to AIRS. Conversely, waves traveling downwind will be more difficult to detect. This visibility effect may explain the east–west asymmetry in the wave pattern observed in Fig. 1. During this study the stratospheric winds are generally westward because of the phase of the QBO and the summer season. Waves traveling to the east are then easily visible, but those traveling to the west are refracted to shorter vertical wavelengths and some may not be visible at all.

Different wave frequencies also travel at different speeds so that the waves observed by AIRS depend on the time interval between the convective source triggering the waves and the AIRS observation. Some of the waves generated by the convection below may have already propagated above the altitude of the AIRS observation.

b. Forward model of AIRS radiances

The wave pattern is visible in the AIRS radiances but not in temperatures of the NASA operational retrievals because of the degradation in resolution during the retrieval process. However, the model we use simulates a temperature field. To compare the AIRS image and the model data we have used the fast forward model called Juelich Rapid Spectral Simulation Code, or JURASSIC (Hoffmann 2006), to simulate AIRS radiance measurements based on the temperature field produced by the model.

JURASSIC computes the radiative transfer based on the Curtis–Godson approximation (CGA) and the emissivity growth approximation (EGA) (e.g., Gordley and Russell 1981; Marshall et al. 1994). Improvements in the accuracy of the JURASSIC forward model are achieved by applying a linear regression scheme that utilizes the EGA and CGA radiances as well as channel-dependent radiometric offsets and linear gain factors as error predictors. For the particular AIRS channel used in this study (channel 75), the forward model error is below 0.15%. This is a factor of 10 below the AIRS measurement noise. In comparison to line-by-line reference calculations, the JURASSIC model is about a factor of 1000 faster.

The JURASSIC forward model provides flexible handling of different types of observation geometry and atmospheric input data. For this research JURASSIC was adapted to the specific requirements of the AIRS measurement geometry and the input temperature field from the model. Details of the forward model as used in this study are given in Hoffmann and Alexander (2009). A flexible ray-tracing algorithm (Hase and Höpfner 1999) allows JURASSIC to exactly determine the lines of sight for the individual AIRS footprints. The 3D model temperature field used as input for JURASSIC is interpolated on the AIRS lines of sight. The radiances produced by JURASSIC are output on the AIRS footprint grid, which has a much lower resolution than the model.

3. Model of waves generated by convection

The model used for this study is a three-dimensional, nonlinear, nonhydrostatic cloud-resolving model that is capable of fully representing atmospheric motions ranging in scale from several tens of meters to several hundred kilometers. The version of the model we are using has been applied previously in numerous studies of waves generated by convection (Piani et al. 2000; Alexander et al. 2004, 2006). The model equations are available in Durran and Klemp (1983) and Piani et al. (2000).

The model has a radiation condition imposed at the top boundary and an open, wave-permeable lateral boundary condition (Durran et al. 1993). For this study we have set the gravity wave outflow speed for the boundary condition to 70 m s^{-1} and the top boundary of the model at 70 km. Wave amplitudes grow very large at these high altitudes, and some reflection of waves can occur because of imperfections in the boundary conditions. To reduce lateral wave reflections near the top of the model, a Rayleigh damping sponge layer is used. With this scheme, values are selected for

the height above which damping begins and for the coefficient that determines the magnitude of the damping τ. Since we are interested in the region between 40 and 45 km for comparison to the AIRS measurement, we begin damping at 55 km and set $\tau = 0.006$ s^{-1}. Damping increases following a cosine shape from zero damping at the initial height (55 km) to damping of half the value of τ at the height halfway between the initial damping height and the top of the model box (i.e., at 62.5 km in this case). Above this point the damping increases linearly, from $\tau/2$ to a maximum value of $\tau/2(1 + \pi/2)$ at the top of the model.

Moist processes are neglected in the model and the initial water vapor profile is set to zero. Waves are forced by heating that varies both spatially in all three dimensions and temporally. The heating is derived from measurements by a scanning research radar located at Gunn Point, Australia (Keenan et al. 1998). This heating field is described in section 3b. The domain size is 760 km × 760 km, with a horizontal resolution of 2 km. The vertical resolution is 0.25 km, which remains constant with height. The model domain is centered on the location of the Gunn Point radar, which is 12.25°S, 131.04°E.

a. Comparison day

A clear wave pattern was observed in the AIRS granule collected at 1640 UTC 12 January 2003 in the region near Darwin. This corresponds to 0210 LST (local standard time) on 13 January in Darwin, since Darwin is 9.5 h ahead of UTC. The waves were observed in both the AIRS 15- and 4-μm bands, but we have used the 15-μm band since the kernel function is sharper in this band. The broader kernel functions of the 4-μm bands mean that information is included from altitudes near the top of the model and we want to avoid this because of the damping imposed near the model lid. Hoffmann and Alexander (2009) discuss the relative sensitivity of the two bands. The full AIRS granule was shown in Fig. 1 for channel 75 in the 15-μm band.

The Australian Bureau of Meteorology (BOM) reports that an unnamed tropical low passed over Elcho Island around 5 January and made landfall as a category-1 tropical cyclone on the Northern Territory coast east of Milingimbi Island. The system drifted into the southwest Gulf of Carpentaria by 12 January LST. In the early morning of 13 January, Darwin time, a line of storms produced flash flooding and wind damage during a 2-h period in Darwin's suburbs and rural area. The BOM rain gauge at Darwin Airport recorded 93 mm of rain in one hour and 24-h totals included 184 mm at Shoal Bay (about 8 km southeast of Gunn Point) and 179 mm at Berrimah (7 km southeast of Darwin Airport).
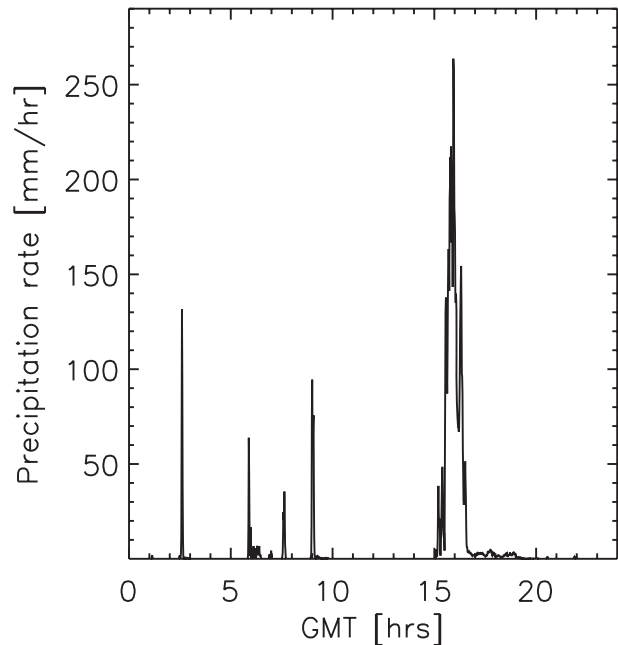

FIG. 3. One-minute rainfall measurements from the ARM rain gauge in Darwin on 12 Jan 2003.

Rainfall measured each minute by an optical rain gauge located at the Atmospheric Measurement Program's Tropical Western Pacific (ARM-TWP) site in Darwin (at 12.425°S, 130.891°E) is shown in Fig. 3. A period of heavy rainfall due to the line of storms associated with the tropical low can be seen between 1500 and 1700 UTC, which corresponds to a local time of between 0130 and 0330 LST on the morning of 13 January. While this is certainly a very strong rain event, the extreme values seen in Fig. 3 may be too high because of bias in the optical rain gauge during heavy rain (Nystuen 1999). Rain rates of greater than 250 mm h^{-1} were reported by the ARM rain gauge while a tipping-bucket rain gauge operated by the BOM and located next to the ARM gauge measured a peak rain rate of 194 mm h^{-1}.

b. Rainfall rates

Forcing for the waves in the model is provided by profiles of latent heating at each model grid location. These profiles are derived from measurements obtained by a C-band polarimetric (C-Pol) radar located at Gunn Point, approximately 20 km north of Darwin and operated by the Australian Bureau of Meteorology. The radar wavelength is 5.3 cm and the peak power is 250 kW (Keenan et al. 1998). A volume scan is completed every 10 min, consisting of conical sweeps at a sequence of increasing elevations. Data are sampled every 300 m out to a range of 150 km and the volume scan is interpolated onto a Cartesian grid.

The range of the C-Pol radar is much smaller than the size of the model domain; it is also circular, in contrast to the square model domain. To prevent a discontinuity in the model input field at the limit of the radar range, the radar measurements are tapered to zero over a few points around the outer edges. The radar data are also interpolated in time from every 10 min to the 2-min resolution used for input to the model.

We use the relationship between precipitation and latent heating to construct heating profiles that vary both in time and three-dimensionally in space with the radar measurements. At each C-Pol grid location the estimates of rainfall rate and precipitation depth are combined to produce a heating profile. Although both rainfall rate and precipitation depth are derived from the C-Pol data, they are not directly linked; while some locations have deep convection and strong heating, others may have deep convection but weak heating. The construction of the heating profiles from the C-Pol measurements is discussed in more detail in section 3d.

The depth to which precipitation extends, Z_{top}, is estimated directly from the gridded 3D volumetric radar measurements of reflectivity. For each grid location, Z_{top} is calculated as the altitude where the radar measurement falls below 6 dBZ; this is used as the maximum altitude for the precipitation at that location. The largest value of Z_{top} in the dataset is just over 19 km, with values between 11 and 15 km being most common during the time of the model run (an example of a Z_{top} field is shown in the grayscale of Fig. 9).

Column rainfall rates are obtained from the reflectivity, differential reflectivity, and specific differential phase using algorithms described by Bringi et al. (2001, 2004). These algorithms are considerably more accurate than conventional radar. The algorithms are less sensitive to variations in drop-size distributions and account for attenuation of the sampled reflectivity and hail contamination. The rainfall rates are gridded to a 128 × 128 array with 2 km × 2 km resolution. The rainfall can be differentiated by type of rain; Fig. 4 shows the areally averaged rainfall for 12 January in green as well as the amounts of convective (red) and stratiform (blue) rain. The rainfall rates are smaller in this figure than in Fig. 3 because the rainfall in Fig. 3 is a point measurement from a rain gauge whereas Fig. 4 shows the radar rainfall averaged over the 65 000 km^2 measurement area.

c. Rainfall measurement discussion

Accurate rainfall estimates are important since the rainfall is used to calculate the vertical heating profiles that force the waves in the model. As a check of our C-Pol rainfall rates, we show in Fig. 5 the C-Pol measurements from the 2 km × 2 km cell over Darwin and
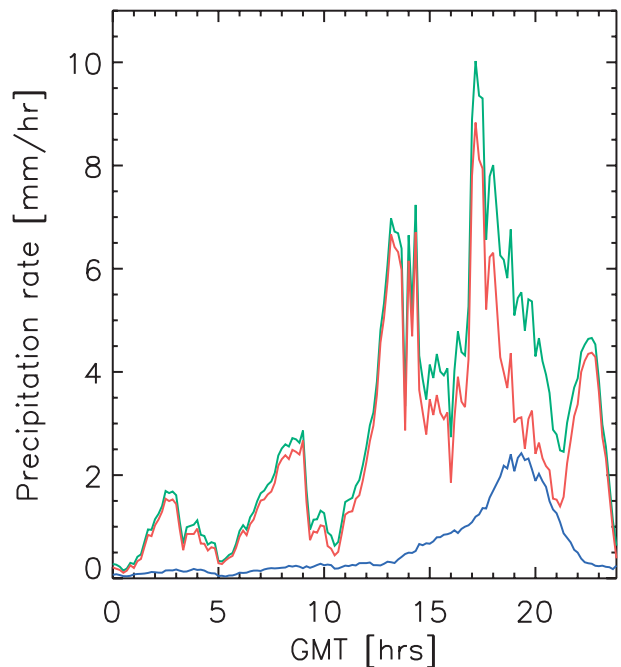

FIG. 4. Rain rate measured by the C-Pol radar, averaged over the radar measurement area, is shown in green. The rain rate separated by rain type is also shown with convective rain in red and stratiform rain in blue.

the rain gauge measurements from the ARM-TWP site in Darwin (the same data as in Fig. 3). This figure shows a considerable discrepancy between the two measurements, particularly at higher rainfall rates. The C-Pol rainfall is lower and smoother than the rain gauge observation, which is significant since it is the C-Pol measurement we are using to determine the model heating, but the features that are most important for gravity wave forcing are the shorter-term rainfall peaks.

One reason for the disagreement between the two measurements is the different time scales over which the C-Pol and rain gauges accumulate data. The optical rain gauge makes continuous measurements that are sampled once per second, and these values are averaged each minute, whereas each C-Pol scan takes 10 min, so the C-Pol cannot be expected to capture the short-term variability seen in the rain gauge record.

Radar and rain gauge comparisons are a common method of validation, but there are several sources of uncertainty that can influence the measurements. One major source of noise is the fact that the rainfall is often not uniform within a radar grid cell. This can cause inconsistencies between the two measurements, but generally not a systematic bias, as whether the rain gauge records more or less rain than the radar depends on the location of the heaviest rain relative to the gauge. This effect is well known (Hendrick and Comer 1970) and
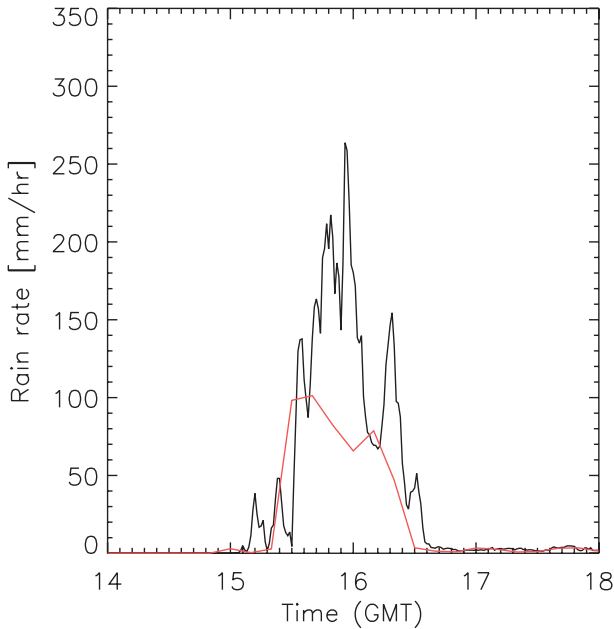
FIG. 5. The Darwin ARM-TWP 1-min rain gauge measurement for 12 Jan 2003 (black) and the C-Pol radar 10-min rain rate for the grid point closest to the rain gauge location (red).

can be quite large; for example, Anagnostou et al. (1999) estimate that for hourly rainfall measurements the uncertainties due to the subgrid rainfall variability contribute up to 60% of the observed differences between the gauge and the radar.

Aside from the rainfall variability, other possible sources of discrepancies between the rain measurements include the scanning pattern of the radar, the radar–rainfall conversion algorithm, and heavy rain and changes in the shape of the drop size distribution, which can influence the optical rain gauge. These effects can lead to a bias in the measurements, rather than a random error.

A study by Nystuen (1999) compared rain measurements from six different types of rain gauge systems: capacitance, weighing, tipping-bucket, optical scintillation, underwater acoustical inversion, and a disdrometer. He found that optical rain gauges were generally biased high during extremely heavy rainfall with high total drop counts, and low at the start of a large convective event when very large drops are often present. The average bias was estimated to be less than 10% but, as shown in his Fig. 13, for the optical gauge the bias increases with increasing rain rate. For a mean rainfall rate of 200 mm h^{-1}, the optical rain gauge measured a rain rate of 250 mm h^{-1}, giving a bias of ~25%. As mentioned earlier, a tipping-bucket gauge collocated with the ARM optical rain gauge measured peak rain rates of 194 mm h^{-1}, which also suggests a potential high bias of ~25%. Research by Krajewski et al. (1998) also showed that optical

rain gauges measured larger rainfall rates than tipping-bucket gauges, even after accounting for wind-induced error of the tipping-bucket mechanism.

The scanning pattern of the radar may be a source of low bias in the radar rainfall. The C-Pol radar measures the rainfall within a large volume around the radar location. This is achieved by using a 1° beamwidth and scanning the measurement volume. Each scan takes 10 min so the C-Pol may miss short-term variability in rainfall rates. In particular, we can see some short duration periods of heavy rainfall in the rain gauge that are underestimated in the radar data, leading to a reduced estimate of the rainfall rate.

Finally, it is known that the conversion from the radar measurement to the rainfall rate is imprecise. Variability of the drop size distribution is a major source of error in this calculation. As mentioned, we have used an algorithm that minimizes this problem, but there remain imperfections in the conversion. We estimate the uncertainty in rain rate due to the conversion to be approximately 30%–50%, which is much improved from the uncertainty of conventional radar rainfall, which is about 100%.

The largest-amplitude waves observed in the AIRS image have horizontal wavelengths of ~50 km. Short duration, large-amplitude rain events tend to produce the largest-amplitude waves at these scales. Short duration events are therefore more relevant to the gravity wave generation than hourly rain amounts or weak rain events. The coarser-resolution C-Pol radar often underestimates such short duration rain events. We compared rain events measured by the C-Pol and rain gauge for additional days in January, using only large-amplitude rain events, selected as those with rain rates greater than 25 mm h^{-1}. This threshold value was chosen by considering the peak rainfall in Figs. 3 and 5, which is about 250 mm h^{-1}. Since the noise in AIRS limits the observation to waves with amplitudes about 10 times smaller than we see during this event, we used the threshold value of 25 mm h^{-1}, which is 10 times smaller than the peak rain. The C-Pol reports 9 such events, while the rain gauge records 42. This difference is due to the C-Pol rainfall not reaching the threshold of 25 mm h^{-1}, rather than the C-Pol missing the event entirely. For these large rainfall events the mean C-Pol rain rate is 52 mm h^{-1}, and the mean for the rain gauge is 70 mm h^{-1}.

d. Conversion of surface rain rates to heating profiles

A vertical profile of heating is constructed at each model grid location using the rainfall rate derived from the C-Pol measurements and the precipitation depth Z_{top}. The shape of the heating profile is dependent on the type of rainfall, with a half sine shape profile considered

most representative for convective rainfall and a full sine shape most representative for stratiform rain (Shige et al. 2004). From Fig. 4 it is clear that in our case the rainfall is largely convective so the use of a half sine heating profile is appropriate. The profile of heating as a function of height $Q(z)$ is then given by

$$Q(z) = \frac{\pi}{2} H_c \sin\left(\frac{\pi z}{Z_{\text{top}}}\right), \tag{1}$$

with $Q(z) = 0$ for $z > Z_{\text{top}}$.

The column heating H_c is calculated from the rainfall rate by assuming that the precipitation heats the air in the column through the release of latent heat during condensation. We have neglected ice phase precipitation and evaporation in the column; this may be a significant source of error in our heating rates and is discussed further in section 5. The column heating is calculated using Eq. (2), where the numerator describes the amount of energy released when the precipitation condensed and the denominator describes how much that energy heated the air in the column (Tao et al. 1993):

$$H_c = \frac{\text{RR}\rho L_c}{C_p M}. \tag{2}$$

Here RR is the rainfall rate as given by the C-Pol radar, ρ is the water density, L_c is the latent heat of condensation, C_p is the heat capacity of air, and M is the column-integrated density of the air below Z_{top}, weighted by the half sine shape assumed for the heating profile. Small changes in the shape of the heating profile can have a relatively large effect on the amplitude of the heating since at higher altitudes the air is more easily heated because of the lower air density. (This effect is illustrated in Fig. 11.)

With the heating profiles calculated using Eqs. (1) and (2), the model produced waves with amplitudes much smaller than the waves observed by AIRS. Comparison between the modeled and observed wave amplitudes showed that good agreement was achieved by increasing the heating profile by a factor of 3.8. This discrepancy is likely due to uncertainties both in the conversion from reflectivity to rain rate, as discussed earlier, and in the conversion from rain rate to heating rate, which will be discussed in more detail in section 5. The results shown in section 4 use the heating rate multiplied by 3.8 as the input forcing field.

e. Initial vertical profiles

The model requires initial vertical profiles of potential temperature θ and the horizontal wind components u and v. For this research we used modified profiles from the European Centre for Medium-Range Weather Forecasts (ECMWF). The initial profiles for the model input are produced by averaging all the ECMWF noon profiles for 12 January 2003 that are within 5° in latitude and longitude of the location of the center of the model. For θ and v we were able to simply extrapolate these average profiles from the top of the ECMWF data at 64.5 km to the top of our model at 70 km. However, the profile of u contained a very strong westward jet, with speeds up to 85 m s^{-1} at 50 km, dropping back below 60 m s^{-1} above 60 km. To retain this jet would require the use of a much finer time step than is necessary for the rest of the model. Since the AIRS kernel function peaks at around 41 km, meaning that the higher altitudes have weaker influence on the observed wave pattern, we used the ECMWF average profile up to 44 km and above this altitude kept the wind speed constant.

These background fields are horizontally uniform and vary only with altitude over the model domain. The profiles used as input to the model are shown in Fig. 6.

f. Model startup

To reduce spurious waves generated by the model at startup, we initialized the model with a zero heating field that was linearly increased over an hour to the strength and pattern of the heating field observed at 1530 UTC. After this time the pattern and strength change according to the observations. In Fig. 4, a period of substantial rainfall, and therefore heating, can be seen between 1230 and 1430 UTC. Following this there is a period of reduced rainfall that continues until just after 1530 UTC. The C-Pol radar data show that between 1230 and 1700 UTC the heating was not spread evenly over the domain but was mainly in a line stretching diagonally from the southwest of Darwin to the northeast and moving to the northwest. (Figure 9 shows the location of the regions of strongest heating at 1530 UTC.)

The wave events observed in the AIRS image at 1640 UTC were forced by convection occurring after 1530 UTC when the model profiles were allowed to vary. We illustrate this by estimating the wave travel time using the form of the vertical group velocity derived from the linearized fluid equations for the case of high-frequency waves (i.e., where the intrinsic frequency is much larger than the Coriolis parameter; e.g., Fritts and Alexander 2003). In this case the vertical group velocity is given by Eq. (3):
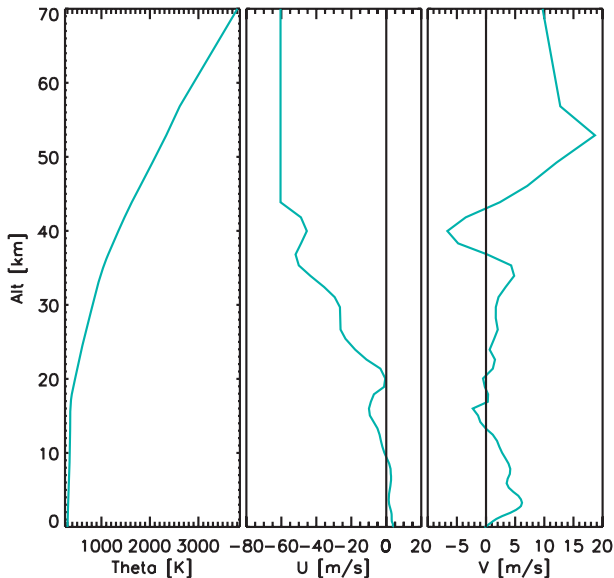
$$C_{gz} = -\frac{Nmk_h}{(k_h^2 + m^2)^{3/2}}, \tag{3}$$

FIG. 6. Vertical profiles of (left) potential temperature, (middle) zonal wind component, u, and (right) meridional wind component, v, used to initialize the model. Vertical lines in the horizontal wind figures are at zero wind speed.

FIG. 7. Temperature (K) output from our model at 1640 UTC and an altitude of 41 km. The Australian coastline is also shown.

where $N = (g\partial \ln\theta/\partial z)^{1/2}$ is the buoyancy frequency, $m = 2\pi/\lambda_z$ is the vertical wavenumber, and $k_h = 2\pi/\lambda_h$ is the horizontal wavenumber. The vertical wavelength λ_z was determined using an S transform on the model output results (Stockwell et al. 1996), while the horizontal wavelength λ_h was estimated by eye from the model output. Values of the vertical wavelength were found to be between 10 and 40 km, while the horizontal wavelengths were estimated at between 45 and 65 km. The time for the waves to travel from the tropopause to the altitude of the AIRS measurement (between 40 and 45 km) is approximately 15 min to an hour.

4. Results

The model output temperature field at 1640 UTC and an altitude of 41 km is shown in Fig. 7. This is the model altitude and time nearest the AIRS granule over Darwin, which has a nominal time of 1641 UTC. The model temperature field shows a clear pattern of waves, which appear to be propagating in all directions from a source somewhere near Darwin. The exact location of the source cannot be inferred from this figure because of wind shear at lower altitudes, which can alter the wave pattern.

To enable direct comparison between the model output and the AIRS data, the model temperatures at the time of the AIRS granule were converted to radiances using the JURASSIC forward model described in section 2b. The forward model is computed at the reso-
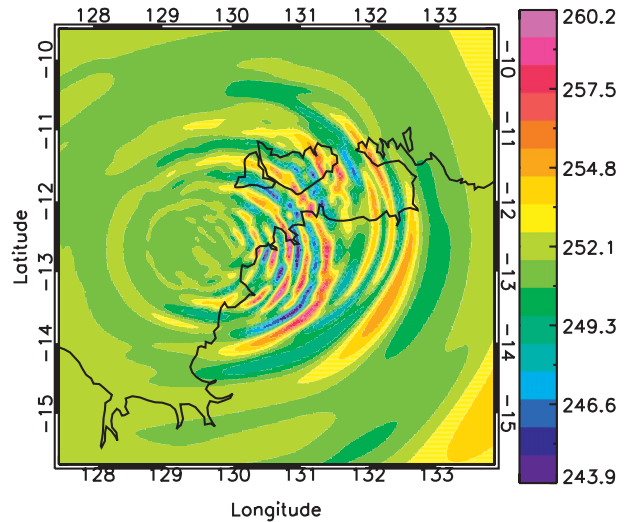
lution of the AIRS granule, and the resulting radiances are shown in the left panel of Fig. 8. The section of the AIRS granule covering the same region as the model output is shown in the right panel of Fig. 8.

In the right panel of Fig. 8, the waves we have modeled can be seen in the eastern half of the domain. These are the largest-amplitude waves in the AIRS granule, with radiances over a range of 10 mW m^{-2} sr^{-1} cm. The curvature of the wave fronts is comparable to that of the waves seen in the model results of the left panel of Fig. 8, which indicates that the source location is similar.

The horizontal wavelengths of the modeled and observed waves are also very similar (50–100 km), and while we adjusted the heating input to achieve corresponding wave amplitudes, the pattern of amplitudes is also similar, with smaller wave amplitudes for the waves farthest east. In the model output of Fig. 7 a complete circle of waves can be seen; in Fig. 8 only a small arc of waves is visible. This difference is due to the vertical resolution of AIRS, which is much coarser than that of the model. As mentioned previously, waves traveling into wind that increases with height are refracted to longer vertical wavelengths. In this case the prevailing wind is from the east so that waves traveling eastward have longer vertical wavelengths and are therefore visible to the AIRS instrument. Waves traveling in other directions have vertical wavelengths below the detection limit for AIRS and are not visible. This effect is reproduced by the forward model so that the waves that are not traveling into the wind are no longer visible in the left panel of Fig. 8.

While the amplitude range is very similar between the observations and the model, the actual radiance values are slightly offset. The model shows positive and negative
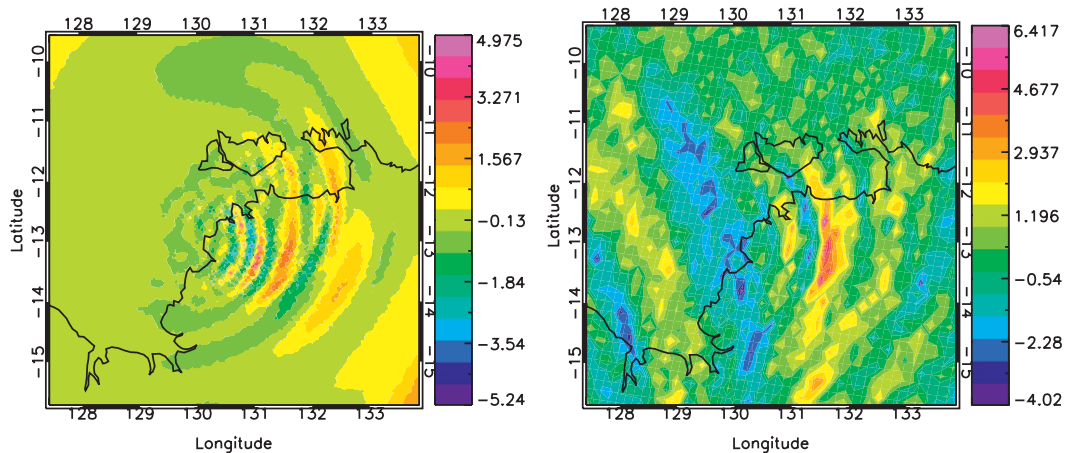
FIG. 8. (left) Radiances produced by passing the model output temperatures through the JURASSIC forward model. These radiances are computed at the same resolution as the AIRS granule and correspond to AIRS channel 75 and an altitude of 41 km, which is the peak of the kernel function for channel 75. (right) The section of the AIRS granule for the same region as at left. Radiances are in units of mW m^{-2} sr^{-1} cm; the coastline of Australia is also shown.

radiances of almost equal magnitude, while the observations have larger positive radiances and smaller negative values. This may be due to the superposition of other waves in the AIRS image from sources outside the C-Pol radar range. An example of such a wave can be seen as larger-scale linear features in the western half of the right panel of Fig. 8 that are absent in the left panel of this figure. As previously mentioned, the curvature in these features suggests a distant source outside the model domain. Similarly, there may be waves from other sources present in the real atmosphere that are not modeled, and also noise in the AIRS measurement, so that overall the AIRS image is not as smooth as the model output.

We have used a heating field derived from measurements by the C-Pol radar to drive the wave production in the model, and in section 3f we estimated that the waves observed at 1640 UTC in both the model and AIRS granule would have been triggered less than an hour beforehand. In Fig. 9 we examine the heating field 50 min before the AIRS overpass, at 1550 UTC. This figure shows the cloud extent in grayscale and the points of maximum heating with color contours. The regions of higher cloud, which are whiter, are in the central and southwest part of the storm, indicating strong convection in these areas. The overlaid color contours show only the regions of strongest heating, where the column heating rates were greater than 0.04 K s^{-1}. These illustrate that the heating is concentrated in very specific locations, mainly within the areas of high clouds. The wave origin was seen in both panels of Fig. 8 to be in the Darwin region, and in Fig. 9 we see from the C-Pol heating field at this earlier time that the Darwin

region contained several well-defined regions of strong heating.

The similarity of the modeled wave structure to the observations, where the model was driven only by the convective heating associated with the tropical storm, indicates that this heating from the tropical storm is the source of the observed waves. These figures therefore clearly link the observed waves to a specific convective event.

5. Discussion and conclusions

We have compared the wave field observed by the AIRS satellite to the wave field produced by a numerical simulation that forces the waves with vertical profiles of convective heating. The convective heating was estimated from real-time rainfall measurements using a C-Pol radar. Feature-for-feature comparison of the modeled and observed wave fields was possible because of our ability to use a heating field in the model which varied in real time both spatially and temporally, and also through the use of a modified version of the JURASSIC forward model, which enabled us to convert the model output temperature field to a radiance field at the same resolution as the AIRS granule. The resulting wave fields correspond well, with similar wave patterns and waves of similar amplitudes. The close agreement of the modeled wave field to the observations indicates that latent heating from a specific convective event—a period of heavy rainfall associated with a strong tropical depression—is the major source of forcing for the waves.

One outstanding issue is that the heating field used to drive the model was multiplied by a factor of 3.8 to
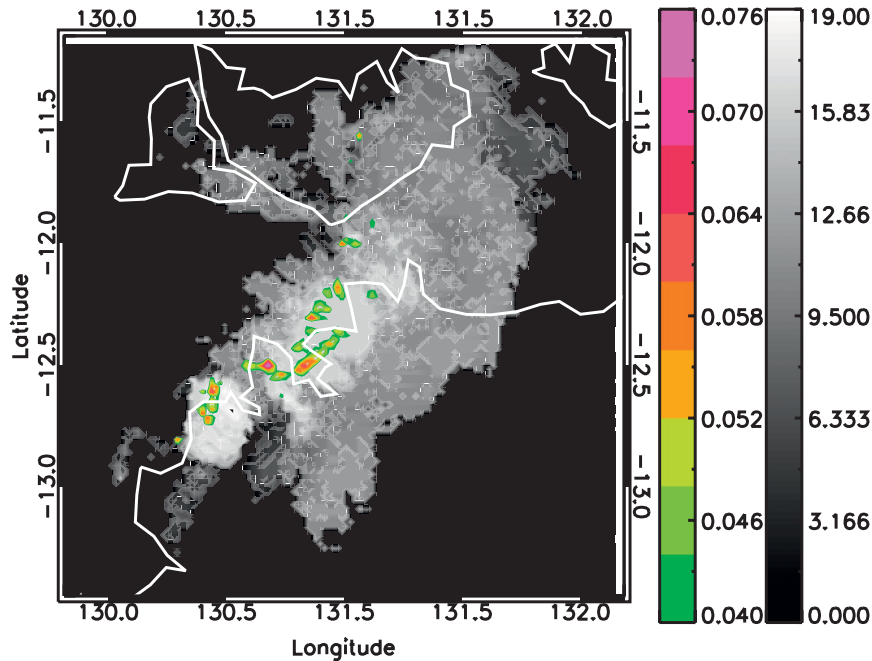
FIG. 9. The grayscale shows cloud-top height (km) as measured by the C-Pol radar at 1550 UTC. Colors show regions of strong heating (heating rates above 0.04 K s^{-1}) as input to the model (i.e., multiplied by 3.8). Although the cloud cover is extensive, the region of strong heating is much smaller and is mainly near Darwin.

increase the amplitude of the modeled waves and reach good agreement with the AIRS observation. We have discussed several sources of uncertainty associated with the C-Pol measurements and the conversion from reflectivity to rainfall, which may lead to differences between the measured rainfall and the actual rainfall and thereby to discrepancies between the model input heating field and the heating driving the waves in the real atmosphere.

Apart from the measurements, we also mentioned that the heating rate calculation considered only the latent heat released by the formation of raindrops and did not include any contribution from the formation of ice. However, Fig. 10 shows that ice phases were observed in localized regions (shown by colors other than blue and gray) at the time the waves were generated. The inclusion of ice in the profile would further increase the amount of heat released and the amplitude of heating. The effect on the heating is much larger than just the additional latent heat of fusion because ice tends to form at higher altitudes where the air density is less, and it melts at lower altitudes where air density is greater. These processes affect the shape of the profile, weighting it toward higher altitudes and also increasing the peak value of the heating without affecting the surface rain rate. Evaporation in the lower troposphere can have an even larger effect because of the larger latent heat of condensation/evaporation. Figure 11 illustrates how the

same surface rain rate can give very different heating values depending on the assumptions made about ice formation and melting. The increase in peak heating amplitude seen in this figure is around 75% and even larger values may be reasonable given the modest assumptions used. An increase in the heating rates input to the model would reduce the multiplication factor of 3.8 that was needed to match the model wave amplitudes to the AIRS observations.

As mentioned, another factor that could influence the amplitude of the waves produced by the model is that evaporative cooling is not included in the model. As described by May and Rajopadhyaya (1999), the downdrafts associated with convective rain can lead to evaporation and therefore the formation of a pool of cold air. This would lead to a larger temperature gradient than that currently produced by our model and possibly to increased wave amplitudes. However, most of the cooling would be in a shallow layer near the surface, whereas the forcing for the observed waves must be deep to explain their long vertical wavelengths (Holton et al. 2002). The absence of cooling is therefore not expected to have a large effect on the modeled waves. The effect of the relative positions of the heating and low-level cooling on the large-scale structure of squall lines has been studied by Pandya and Durran (1996). They found that while gravity waves will not be directly affected by
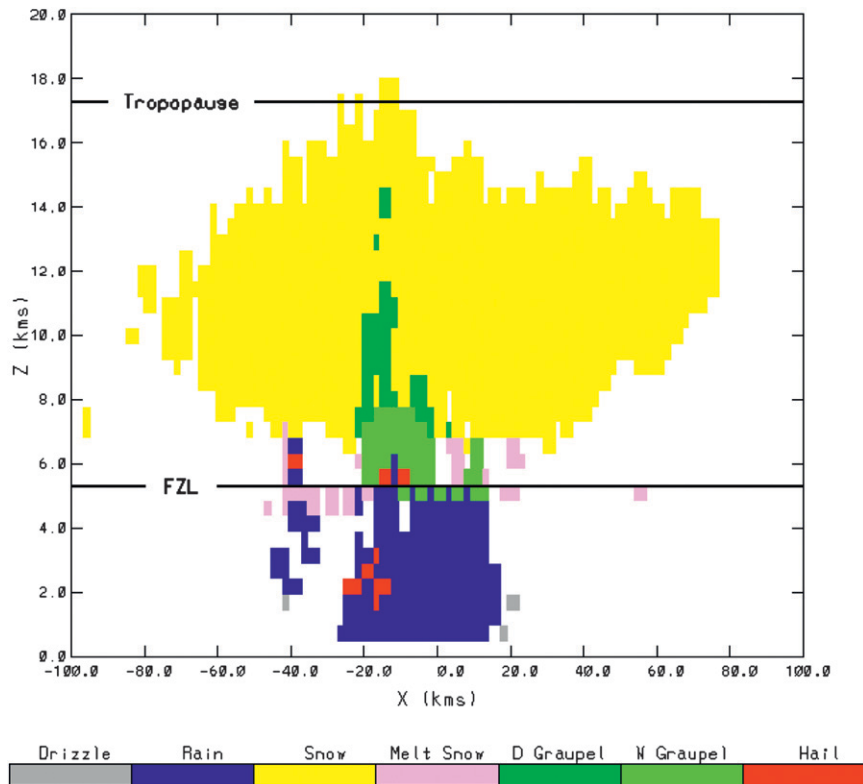
FIG. 10. Cross section of C-Pol data near Darwin (17.5 km south of Gunn Point) at 1550 UTC 12 Jan 2003 showing the precipitation classification. Dry and wet graupel are shown separately as D and W Graupel. The freezing level is at 5.3 km, and the tropopause at 17.3 km.

a change in the position of the low-level cooling, the tropospheric winds may be affected, and these may influence the gravity waves.

May and Ballinger (2007) have classified convection in the Darwin region into monsoon and break conditions. Monsoon storms generally have weaker convection and more rain, especially stratiform rain, whereas break storms have strong vertical motion and the cells often reach and overshoot the tropopause. The wet season in Darwin is between October and April, and while monsoon and break conditions are interspersed during this time, monsoon conditions dominate during January and February.

The vertical velocity profiles in each of these convection categories were examined by Wu et al. (2009), who found that break profiles had maximum vertical velocities of up to almost 40 m s^{-1} and peaked at higher altitudes than the monsoon profiles (see their Fig. 3). As a way of evaluating whether the increased heating input to our model was producing physically reasonable results, we compared these results to the updraft speeds from our model during the time at which we estimate the waves were generated (1550 UTC). A profile of vertical velocity was constructed using only locations where the

rainfall rate was in the top 10% of values over the domain, a total of 12 profiles. These are the locations we expect to have triggered the waves we are investigating. We found that the vertical velocity peaked in the upper
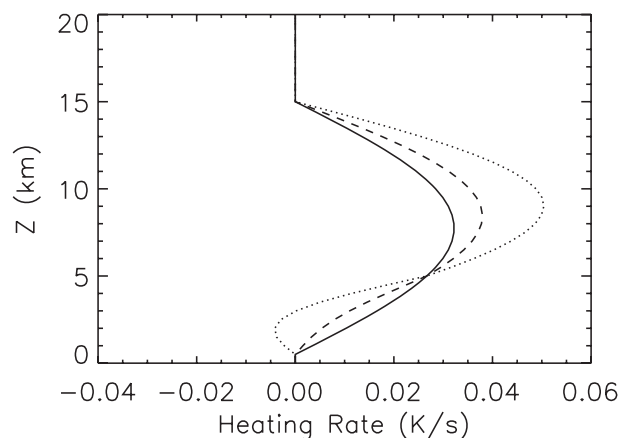

FIG. 11. Local profile of latent heating in a 100 mm h^{-1} deep convective rain event. The solid line shows the heating profile assuming only moist rain with no evaporation. The dashed line shows the profile assuming ice above the melting layer, and the dotted line shows the effect of assuming that 30% of the rain in the column evaporates below 5 km.
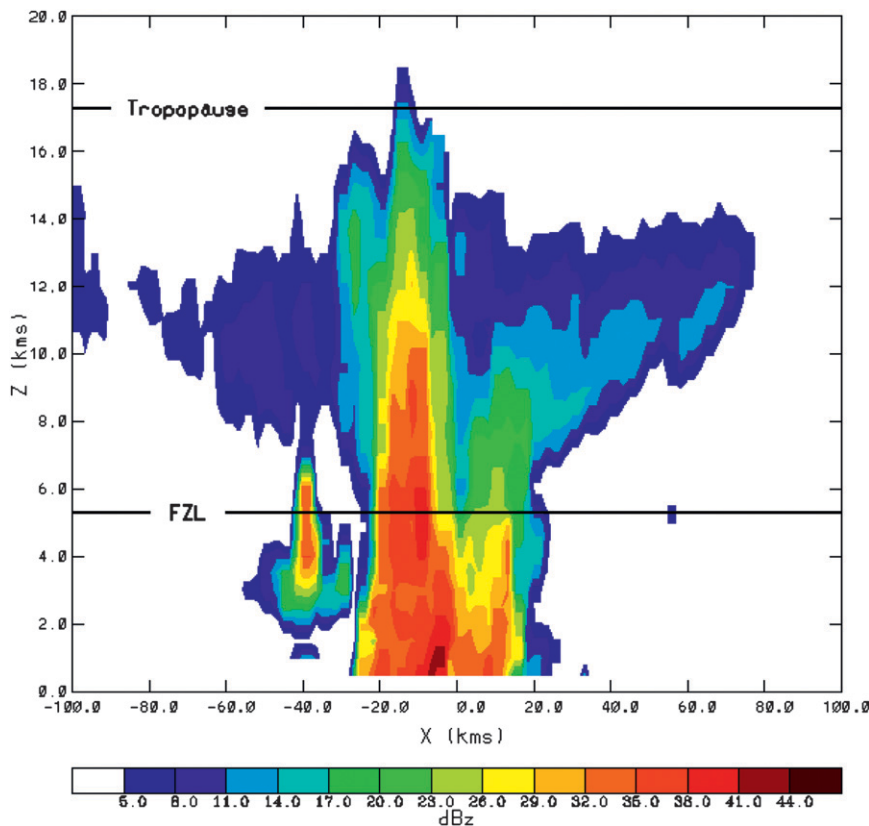
FIG. 12. As in Fig. 10, but showing the radar reflectivity.

part of the troposphere with values of almost 30 m s^{-1}. Although this storm occurred in January when monsoon conditions are expected to prevail, the profile corresponds very well to the profile shape given by Wu et al. (2009) for break conditions. The radar reflectivity along an east–west cross section over Darwin is shown in Fig. 12. This figure also indicates that the storm was characteristic of a break-period storm since it overshoots the tropopause (located at about 17 km), has a large region of intense radar reflectivity, and has a significant amount of ice phase hydrometeors in the upper troposphere. This comparison shows that forcing the model with increased heating produces results that are physically reasonable and consistent with the properties of the type of storm observed at this time.

The shape used for the vertical profile of heating was a positive half sine wave, a shape that corresponds better to convective heating than stratiform heating and which has been used in several earlier studies (Bretherton 1988; Mapes 1993). Alexander and Holton (2004) point out that the shape of the profile is not as important as the correct horizontal distribution of the heating. However, we have not investigated this question since in this case a large proportion of the rainfall was convective, so the vertical heating profile should be well represented by

a half sine shape. In cases with more stratiform rain it may be necessary to refine the vertical profile since the half sine shape is not a suitable model for stratiform heating (Shige et al. 2004).

Neither the AIRS image nor the model can capture all the waves present in the atmosphere. The model does not include any waves that were not generated within the radar scan area, while the AIRS observation has limited horizontal and vertical resolution. For consistency with the observed wave field we have downgraded the model resolution to match that of the AIRS granule. As can be seen from the comparison between Figs. 7 and 8, this degradation in resolution means that many of the structures in the northern region that are quite clear in the high-resolution model output of Fig. 7 are no longer visible when the resolution is downgraded to that of the AIRS image. An improvement in instrument spatial resolution would allow more of these small-scale wave structures to be observed. The direction of the prevailing wind also influences the wavelengths that can be resolved since waves traveling into the prevailing wind are refracted to longer vertical wavelengths and so become more visible to AIRS.

The AIRS overpass at 1640 UTC occurred within an hour after a large-amplitude rain event over Darwin, and

the satellite observed the large-amplitude wave event that was generated. According to the C-Pol radar data (Fig. 4), several other large-amplitude rain events occurred earlier in the day within the radar area, followed by a relatively quiet period and then by the event that was observed. The waves from these earlier events would have long since propagated to altitudes above the AIRS 40-km observation level. AIRS overpasses occur only twice daily for tropical and midlatitude locations. Twice-daily sampling coupled to the intermittent nature of convective sources and the fast vertical group speeds of the waves visible to AIRS will likely mean many of these events will be missed by the satellite, and some serendipity of the satellite being in the right place at the right time may be needed. In fact, the 0130 and 1330 local time equatorial crossings of the satellite are not very well phased with the diurnal cycle of convection for the purpose of observing convectively generated waves. A peak in the diurnal cycle over land occurs in the late afternoon and another peak over the tropical ocean occurs in the postmidnight-to-predawn morning hours (Chen and Houze 1997). Thus, while large-amplitude wave events such as the one in this paper may be relatively rare in the AIRS data, they may not be nearly so rare in nature.

To estimate the significance of this wave event observed by AIRS, we have computed wave momentum fluxes in the model lower stratosphere at 20 km, below the strong westward shear zone. The winds at this level are weak (<3.5 m s^{-1}), and the wave field is more nearly isotropic in azimuth. The fluxes at this altitude can be compared to other studies describing convective wave fluxes entering the stratosphere (e.g., Baldwin et al. 2001). Local maximum values of the momentum flux are approximately 0.06–0.14 Pa, comparable to local values above convection seen in previous observations (Sato 1993; Alexander et al. 2000; Wang et al. 2006). We also compute the domain average momentum flux from the cospectrum of horizontal and vertical wind perturbations multiplied by density (Alexander et al. 2004). The absolute value of the fluxe averaged over a $4° \times 4°$ central area of the model domain is 5 mPa, a value comparable to the zonal-mean, time-mean momentum fluxes needed to drive the QBO. Only roughly half of the flux in this case is zonally propagating, and a source like this is not only localized but also sporadic in time. This is, therefore, a significant but not highly unusual convective gravity wave event.

This research has linked a specific convective event to waves observed in the stratosphere through the use of a 3D model driven by real-time heating profiles. The conversion from reflectivity to heating still requires improvement, which means the wave amplitudes produced by the model are uncertain, but the horizontal and vertical wavelengths as well as the wave pattern are very similar to those observed by AIRS.

REFERENCES

Alexander, M. J., and J. R. Holton, 2004: On the spectrum of vertically propagating gravity waves generated by a transient heat source. *Atmos. Chem. Phys.,* **4,** 923–932.

——, and C. Barnet, 2007: Using satellite observations to constrain parameterizations of gravity wave effects for global models. *J. Atmos. Sci.,* **64,** 1652–1665.

——, J. R. Holton, and D. R. Durran, 1995: The gravity wave response above deep convection in a squall line simulation. *J. Atmos. Sci.,* **52,** 2212–2226.

——, J. H. Beres, and L. Pfister, 2000: Tropical stratospheric gravity wave activity and relationships to clouds. *J. Geophys. Res.,* **105,** 22 299–22 309.

——, P. T. May, and J. H. Beres, 2004: Gravity waves generated by convection in the Darwin area during the Darwin Area Wave Experiment. *J. Geophys. Res.,* **109,** D20S04, doi:10.1029/2004JD004729.

——, J. H. B. Richter, and B. R. Sutherland, 2006: Generation and trapping of gravity waves from convection with comparison to parameterization. *J. Atmos. Sci.,* **63,** 2963–2977.

Anagnostou, E. N., W. F. Krajewski, and J. Smith, 1999: Uncertainty quantification of mean-areal radar-rainfall estimates. *J. Atmos. Oceanic Technol.,* **16,** 206–215.

Baldwin, M. P., and Coauthors, 2001: The quasi-biennial oscillation. *Rev. Geophys.,* **39,** 179–229.

Beres, J. H., R. R. Garcia, B. A. Boville, and F. Sassi, 2005: Implementation of a gravity wave source spectrum parameterization dependent on the properties of convection in the Whole Atmosphere Community Climate Model (WACCM). *J. Geophys. Res.,* **110,** D10108, doi:10.1029/2004JD005504.

Bergman, J. W., and M. L. Salby, 1994: Equatorial wave activity derived from fluctuations in observed convection. *J. Atmos. Sci.,* **51,** 3791–3806.

Bretherton, C., 1988: A theory for nonprecipitating convection between two parallel plates. Part II: Nonlinear theory and cloud field organization. *J. Atmos. Sci.,* **45,** 2391–2415.

Bringi, V. N., G.-J. Huang, V. Chandrasekar, and T. D. Keenan, 2001: An areal rainfall estimator using differential propagation phase: Evaluation using a C-band radar and a dense gauge network in the tropics. *J. Atmos. Oceanic Technol.,* **18,** 1810–1818.

——, T. Tang, and V. Chandrasekar, 2004: Evaluation of a new polarimetrically based *Z–R* relation. *J. Atmos. Oceanic Technol.,* **21,** 612–622.

Charron, M., and E. Manzini, 2002: Gravity waves from fronts: Parameterization and middle atmosphere response in a general circulation model. *J. Atmos. Sci.,* **59,** 923–941.

Chen, S. S., and R. A. Houze Jr., 1997: Diurnal variation and life-cycle of deep convective systems over the tropical Pacific warm

pool. *Quart. J. Roy. Meteor. Soc.,* **123,** 357–388, doi:10.1002/qj.49712353806.

Chun, H.-Y., and J.-J. Baik, 1998: Momentum flux by thermally induced internal gravity waves and its approximation for large-scale models. *J. Atmos. Sci.,* **55,** 3299–3310.

——, M.-D. Song, J.-W. Kim, and J.-J. Baik, 2001: Effects of gravity wave drag induced by cumulus convection on the atmospheric general circulation. *J. Atmos. Sci.,* **58,** 302–319.

Dewan, E. M., and Coauthors, 1998: MSX satellite observations of thunderstorm-generated gravity waves in mid-wave infrared images of the upper stratosphere. *Geophys. Res. Lett.,* **25,** 939–942.

Dunkerton, T. J., 1997: The role of gravity waves in the quasi-biennial oscillation. *J. Geophys. Res.,* **102,** 26 053–26 076.

Durran, D. R., and J. B. Klemp, 1983: A compressible model for the simulation of moist mountain waves. *Mon. Wea. Rev.,* **111,** 2341–2361.

——, M.-J. Yang, D. N. Slinn, and R. G. Brown, 1993: Toward more accurate wave-permeable boundary conditions. *Mon. Wea. Rev.,* **121,** 604–620.

Fovell, R., D. Durran, and J. R. Holton, 1992: Numerical simulations of convectively generated stratospheric gravity waves. *J. Atmos. Sci.,* **49,** 1427–1442.

Fritts, D. C., and M. J. Alexander, 2003: Gravity wave dynamics and effects in the middle atmosphere. *Rev. Geophys.,* **41,** 1003, doi:10.1029/2001RG000106.

Giorgetta, M. A., E. Manzini, and E. Roeckner, 2002: Forcing of the quasi-biennial oscillation from a broad spectrum of atmospheric waves. *Geophys. Res. Lett.,* **29,** 1245, doi:10.1029/2002GL014756.

Gordley, L. L., and J. M. Russell III, 1981: Rapid inversion of limb radiance data using an emissivity growth approximation. *Appl. Opt.,* **20,** 807–813.

Hamilton, K., R. A. Vincent, and P. T. May, 2004: Darwin Area Wave Experiment (DAWEX) field campaign to study gravity wave generation and propagation. *J. Geophys. Res.,* **109,** D20S01, doi:10.1029/2003JD004393.

Hase, F., and M. Höpfner, 1999: Atmospheric ray path modeling for radiative transfer algorithms. *Appl. Opt.,* **38,** 3129–3133, doi:10.1364/AO.38.003129.

Hendrick, R. L., and G. H. Comer, 1970: Space variations of precipitation and its implications for rain gauge networks. *J. Hydrol.,* **10,** 151–162.

Hoffmann, L., 2006: Schnelle Spurengasretrieval für das Satellitenexperiment Envisat MIPAS. Tech. Rep. JUEL-4207 ISSN 0944-2952, Forschungszentrum Jülich, 143 pp.

——, and M. J. Alexander, 2009: Retrieval of stratospheric temperatures from Atmospheric Infrared Sounder radiance measurements for gravity wave studies. *J. Geophys. Res.,* **114,** D07105, doi:10.1029/2008JD011241.

Holton, J. R., 1983: The influence of gravity wave breaking on the general circulation of the middle atmosphere. *J. Atmos. Sci.,* **40,** 2497–2507.

——, J. H. Beres, and X. Zhou, 2002: On the vertical scale of gravity waves excited by localized thermal forcing. *J. Atmos. Sci.,* **59,** 2019–2023.

Keenan, T., K. Glasson, F. Cummings, T. S. Bird, J. Keeler, and J. Lutz, 1998: The BNRC/NCAR C-Band polarimetric (C-POL) radar system. *J. Atmos. Oceanic Technol.,* **15,** 871–886.

Kershaw, R., 1995: Parameterization of momentum transport by convectively generated gravity waves. *Quart. J. Roy. Meteor. Soc.,* **121,** 1023–1040, doi:10.1002/qj.49712152505.

Krajewski, W. F., A. Kruger, and V. Nespor, 1998: Experimental and numerical studies of small-scale rainfall measurements and variability. *Water Sci. Technol.,* **37,** 131–138.

Kuester, M., M. Alexander, and E. Ray, 2008: A model study of gravity waves over Hurricane Humberto (2001). *J. Atmos. Sci.,* **65,** 3231–3246.

Mapes, B. E., 1993: Gregarious tropical convection. *J. Atmos. Sci.,* **50,** 2026–2037.

Marshall, B. T., L. L. Gordley, and D. A. Chu, 1994: BANDPAK: Algorithms for modeling broadband transmission and radiance. *J. Quant. Spectrosc. Radiat. Transf.,* **52,** 581–599.

May, P. T., and D. K. Rajopadhyaya, 1999: Vertical velocity characteristics of deep convection over Darwin, Australia. *Mon. Wea. Rev.,* **127,** 1056–1071.

——, and A. Ballinger, 2007: The statistical characteristics of convective cells in a monsoon regime (Darwin, Northern Australia). *Mon. Wea. Rev.,* **135,** 82–92.

Nastrom, G. D., and K. S. Gage, 1985: A climatology of atmospheric wavenumber spectra of wind and temperature observed by commercial aircraft. *J. Atmos. Sci.,* **42,** 950–960.

Nystuen, J. A., 1999: Relative performance of automatic rain gauges under different rainfall conditions. *J. Atmos. Oceanic Technol.,* **16,** 1025–1043.

Pandya, R. E., and D. R. Durran, 1996: The influence of convectively generated thermal forcing on the mesoscale circulation around squall lines. *J. Atmos. Sci.,* **53,** 2924–2951.

——, and M. J. Alexander, 1999: Linear stratospheric gravity waves above convective thermal forcing. *J. Atmos. Sci.,* **56,** 2434–2446.

Piani, C., D. Durran, M. J. Alexander, and J. R. Holton, 2000: A numerical study of three-dimensional gravity waves triggered by deep tropical convection and their role in the dynamics of the QBO. *J. Atmos. Sci.,* **57,** 3689–3702.

Ricciardulli, L., and R. Garcia, 2000: The excitation of equatorial waves by deep convection in the NCAR Community Climate Model (CCM3). *J. Atmos. Sci.,* **57,** 3461–3487.

Sato, K., 1993: Small-scale wind disturbances observed by the MU radar during the passage of Typhoon Kelly. *J. Atmos. Sci.,* **50,** 518–537.

Shige, S., Y. N. Takayabu, W.-K. Tao, and D. E. Johnson, 2004: Spectral retrieval of latent heating profiles from TRMM PR data. Part I: Development of a model-based algorithm. *J. Appl. Meteor.,* **43,** 1095–1113.

Stockwell, R. G., L. Mansinha, and R. P. Lowe, 1996: Localization of the complex spectrum: The *S* transform. *IEEE Trans. Signal Process.,* **44,** 998–1001, doi:10.1109/78.492555.

Tao, W.-K., S. Lang, J. Simpson, and R. Adler, 1993: Retrieval algorithms for estimating the vertical profiles of latent heat release: Their applications for TRMM. *J. Meteor. Soc. Japan,* **71,** 685–700.

Taylor, M. J., and M. Hapgood, 1988: Identification of a thunderstorm as a source of short period gravity waves in the upper atmospheric nightglow emissions. *Planet. Space Sci.,* **36,** 975–985.

Vincent, R. A., and I. M. Reid, 1983: HF Doppler measurements of mesospheric gravity wave momentum fluxes. *J. Atmos. Sci.,* **40,** 1321–1333.

Wang, L., M. J. Alexander, T. P. Bui, and M. J. Mahoney, 2006: Small-scale gravity waves in ER-2 MMS/MTP wind and temperature measurements during CRYSTAL-FACE. *Atmos. Chem. Phys.,* **6,** 1091–1104.

Wu, J., A. D. D. Genio, M.-S. Yao, and A. B. Wolf, 2009: WRF and GISS SCM simulations of convective updraft properties during TWP-ICE. *J. Geophys. Res.,* **114,** D04206, doi:10.1029/2008JD010851.

Wu, X., and M. W. Moncrieff, 1996: Collective effects of organized convection and their approximation in general circulation models. *J. Atmos. Sci.,* **53,** 1477–1495.